Energy & Environmental Science

Accepted Manuscript

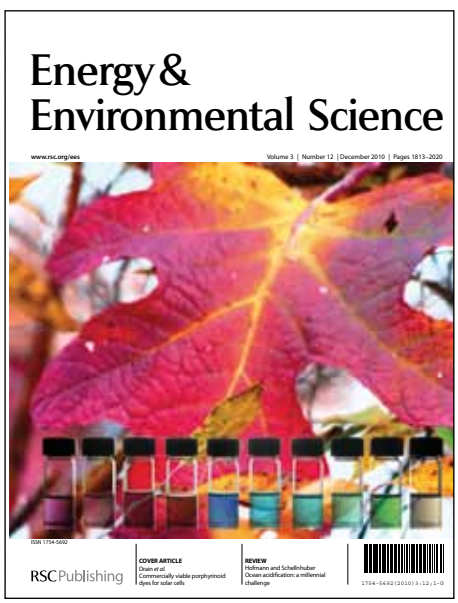

RSC Publishing

www.rsc.org/ees
Registered Charity Number 207890

Cite this: DOI: 10.1039/c0xx00000x

www.rsc.org/xxxxxx

ARTICLE TYPE

Gold Nanoparticles Inlaid TiO_2 Photoanodes: A Superior Candidate for High-Efficiency Dye-Sensitized Solar Cells

Yan Li[†,‡], Hong Wang[†,□], Quanyou Feng[†,□], Gang Zhou[†], *and* Zhong-Sheng Wang*[,†]

Received (in XXX, XXX) Xth XXXXXXXXX 20XX, Accepted Xth XXXXXXXXX 20XX
DOI: 10.1039/b000000x

By designing a fine-controlled nanocomoposite with Au nanoparticles (~ 2 nm in size) directly inlaid in TiO_2 as working electrode, efficiency (η) of 10.1% for a dye-sensitized solar cell with an open-circuit photovoltage of 863 mV and a short-circuit photocurrent of 15.71 mA/cm^2 has been realized, giving an enhancement of 97 mV in photovoltage, 63% in photocurrent and 84% in efficiency compared to the cell with pure TiO_2 photoanode (η = 5.5%). As compared to pure TiO_2, besides the local-field optical enhancement near the TiO_2 surface caused by plasma resonance of Au nanoparticles which increases the dye absorption and hence the amount of photogenerated charge contributing to photocurrent, it is evidenced that not only the quasi-Fermi level of Au-TiO_2 photoanode can be modulated to more negative potentials by controlling the mass ratio of Au/TiO_2, but their mosaic nanostructure reduces the charge recombination rate effectively, both leading to a marked enhancement of photovoltage. Our results prove that the unique nanostructural, physical and chemical properties of the direct mosaic nanoarchitecture of ~ 2 nm Au and TiO_2 make them the valuable materials as working electrode for DSSCs to achieve high photovoltage and hence further improve the performance.

Introduction

Since dye-sensitized solar cell (DSSC) was first reported,[1] it has been a focus of intensive research activities as a promising platform of photovoltaics to produce high-performance solar cells. In the past decades, considerable efforts, including novel sensitizers,[2-7] electrolytes,[8-13] photoanodes[14-19] and also the fundamental understandings,[20-25] have been performed to improve the power conversion efficiency and long-term stability of the DSSCs, and so far, the record efficiency reported for DSSCs is 12.3%.[26]

Surface plasmon resonance from noble metal nanostructures can give rise to unique properties, such as an intense absorption feature and enhanced local electromagnetic field, which have been implemented in nonlinear optical process,[27,28] surface enhanced spectroscopy,[29,30] sensing,[31] optical antennas,[32] photocatalysis[33,34] and organic photovoltaic devices.[35] Recently, employing the surface Plasmon resonance of noble metal nanoparticles (NPs) into DSSCs has been regarded as an attractive approach to boost the performance of DSSCs.[36-39] For most of the previous efforts, by incorporating metal (Ag, Au) particles[40-42] and more often the metal@TiO_2 or metal@SiO_2 core-shell structures[43-45] into flat or porous TiO_2 anode, plasmon-enhanced light absorption of the dye and hence the increased photocurrent have been demonstrated in DSSCs. Nevertheless, decreased efficiencies were also observed upon the incorporation of Au NPs in TiO_2, and attributed to the decreased surface area of the underlying semiconductor in direct contact with the absorbing dye molecules[46] or the poor control over the metal-TiO_2 hetero-structure.[47] Moreover, the decrease in open-circuit photovoltage is also of frequent occurrence offsetting the increase in conversion efficiency. Therefore, to further improve the efficiency of such "Plasmonic DSSCs", the greatest possibilities for efficiency gains are likely to be those that center on increasing the photovoltage meanwhile keeping the plasmonic effect.

In the present study, small Au NPs (~2 nm in diameter) were desinged and fabricated using a cross-linked polymerized ionic liquid as the stabilizer, and were directly inlaid in TiO_2 in a well-controlled manner to construct the working electrode for DSSCs comprising a metal-free organic dye and the typical iodide/triiodide redox electrolyte, as illustrated in Scheme 1. In addition to having the typical plasma-induced dye absorption, such Au inlaid TiO_2 photoanode demonstrates a tunable quasi-Fermi level to more negative potentials by controlling the mass ratio of Au and TiO_2 , that is exactly what we need to further enlarge the photovoltage and hence the efficiency of the DSSCs. Herein, using 4-μm-thick 0.168 wt% (Au/TiO_2 weight ratio, the same below) Au-TiO_2 as photoanode, having a nearly 90 mV negatively shifted quasi-Fermi level, a power conversion efficiency of 10.1 % with open-circuit photovoltage of 863 mV has been achieved, showing 84% increase in power conversion efficiency and 97 mV enhancement of open-circuit photovoltage as compared to that with TiO_2 anode at the same conditions. The physicochemical properties of Au-TiO_2 nanocomposites and their photovoltaic performances as photoanodes in DSSCs have been systematically studied, which would enable us to identify some key aspects of the enhancement mechanism with which the performance of DSSCs is influenced by the Au nanoparticles.

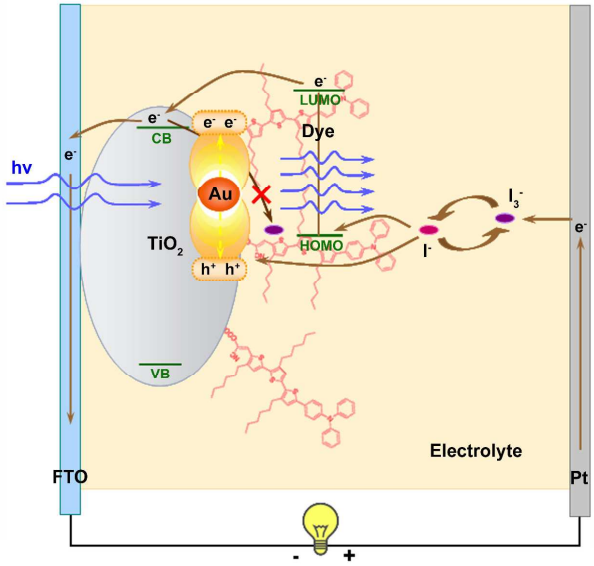

Scheme 1. Schematic illustration of the configuration, surface plasmonic resonance of Au nanoparticles, and charge transfer processes in the DSSC incorporating the Au-TiO_2 photoanode.

Results and discussion

Using a cross-linked polymerized ionic liquid[48] (CLP, Figure S1, see Supplementary Information, SI) as the stabilizer, the prepared Au NPs were ~2 nm in size (Figure S2), having a plasma absorption band centered at 516 nm (Figure S3). Once Au and TiO_2 colloids, whose Zeta potentials were determined to be +7.72 and -9.49 mV for Au and TiO_2 colloids respectively, were mixed together through ultrasonication, the electrostatic effect could make Au NPs be fixed on the surface of TiO_2. In subsequent sintering at 500 °C, CLP decomposed and Au NPs were then nested and inlaid in TiO_2 NPs (denoted as Au-TiO_2). High-resolution transmission electron microscopy (HRTEM) micrographs of Au-TiO_2 nanocomposite are shown in Figure 1. Figure 1a directly demonstrates that the Au NPs (~ 2 nm) are fixed on the TiO_2 NPs (15-20 nm in size) surfaces in a highly dispersed state. Figure 1b reveals that both Au and TiO_2 NPs are highly crystallized as evidenced from the well resolved Au (111) (d = 0.23 nm) and TiO_2 (101) (d = 0.35 nm) crystalline lattices. Partial overlapping of the lattice fringes in Figure 1b clearly indicates the nanoscale mosaic structure of Au and TiO_2. For small Au NPs (e.g. < 3 nm in size), it is reported that gold atoms are preferentially attached to specific sites of TiO_2 surface and form an epitaxial and coherent heterointerface, but gold-TiO_2 interface will lose lattice coherency to accommodate the lattice mismatch between the two dissimilar crystals for larger size of gold NP.[49] Moreover, there is no change of size, morphology and crystalline structure for Au NPs during the preparation of Au-TiO_2 composite, indicating that Au NPs were thermal and structural stable. The polymer stabilizer around Au NPs in colloid might play a key role in protecting Au NPs from aggregation in the process of photoanode fabrication.

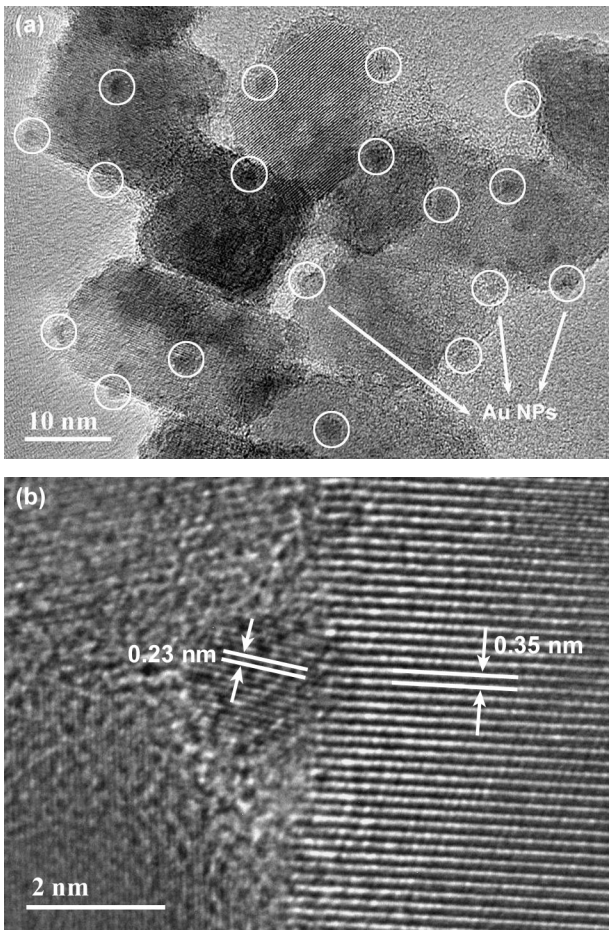

Figure 1. (a) HRTEM image of Au-TiO_2 NPs and (b) lattice fringes of Au-TiO_2 NPs, showing the characteristics of face-centered-cubic (fcc) Au (111) (d = 0.23 nm) and anatase TiO_2 (101) (d = 0.35 nm). The encircled particles are Au NPs (~2 nm). Au/TiO_2 = 0.800 wt%.

The X-ray diffraction (XRD) peaks for a TiO_2 film on glass slide can be well indexed to anatase TiO_2 (JCPDS 21-1272), and an Au NPs film on glass slide exhibits the characteristic (111), (200) and (220) reflections for face-centered-cubic (fcc) metallic Au^0 phase (JCPDS 04-0784), as shown in Figure 2a. These characteristic reflections for fcc metallic Au^0 phase and anatase TiO_2 are both clearly observed in the XRD spectrum of Au-TiO_2 nanocomposite on glass slide. The binding energies of Au $4f_{7/2}$ (83.3 eV) and Au $4f_{5/2}$ (86.8 eV) in high resolution X-ray photoelectron spectroscopy (XPS) (Figure S4) further verified the metallic phase of Au in Au-TiO_2 composite. The shifts of 0.7 eV (from 84.0 eV for pure Au to 83.3 eV for Au-TiO_2 NPs) for $Au4f_{7/2}$ peak is the result of strong interaction between nanosized Au and TiO_2 support via the unique nanoscale heterointerface structure,[34] which may also affect the lattice vibrations of TiO_2. Figure 2b compares the Raman spectra for pure TiO_2 and Au-TiO_2 films. The observed peak located at 143.4 cm^{-1} for pure TiO_2 film belongs to the anatase phase of TiO_2, which is very close to the 144.0 cm^{-1} peak in anatase phase of single crystal.[50] For Au-TiO_2 films, this peak is gradually shifted to higher wavenumber as the Au content increases, demonstrating increased crystalline defects within the TiO_2. For the Au inlaid TiO_2 composite, local lattice distortions, the so called crystalline defects, could be caused at the contact region of Au and TiO_2,

which can influence the characteristic vibrational frequency of the anatase TiO_2 as shown in the Raman spectra (Figure 2b). These crystalline defects can act as traps to capture photoelectrons and then the trapped electrons by the crystalline defects may be detrapped and transport to the collecting electrode for photocurrent generation. Owing to the trapping of injected electrons by the crystalline defects, charge recombination between the injected electrons and triiodides in the electrolyte can thus be inhibited.[34,51-53]

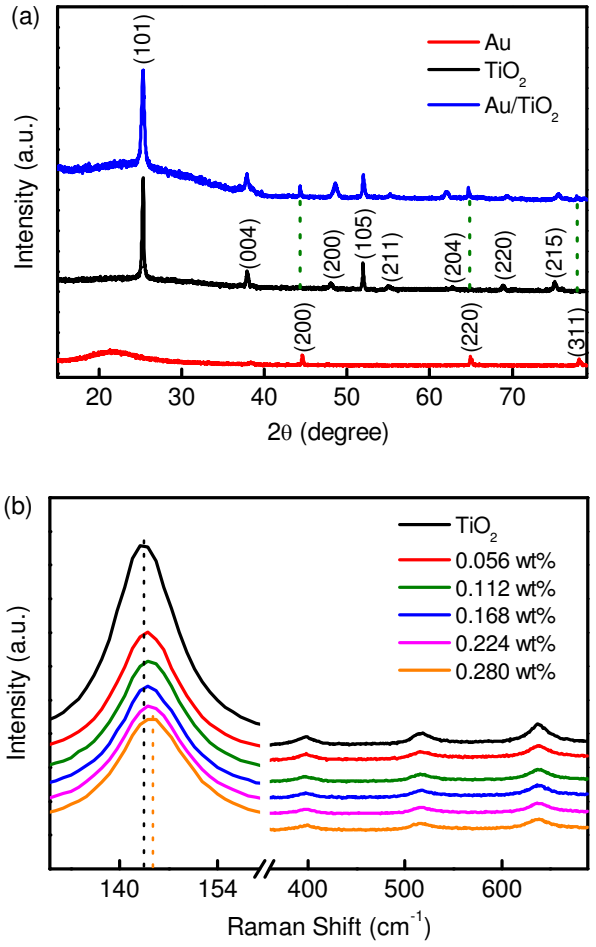

Figure 2. (a) XRD patterns of the Au NPs, TiO_2 and Au-TiO_2 (Au/TiO_2 = 0.800wt%) films and (b) Raman spectra of pure TiO_2 and Au-TiO_2 with various Au loadings

Spherically integrated UV-vis absorption properties of the Au-TiO_2 films (~1 μm) with different Au loadings are shown in Figure 3. It is clear that the absorption of bare TiO_2 film is featureless above 400 nm, but an absorption band centered at ~535 nm is characterized in Au-TiO_2 films and intensifies with the increase of Au amount, which is attributed to the Plasmon resonance absorption peak arising from Au NPs. As compared to the gold colloid in methanol (Figure S3), the plasma band for Au-TiO_2 films are red-shifted and broadened owing to the high refractive index (2.52) of anatase TiO_2.[54] The surface plasmonic resonance created by Au NPs can cause strong local field enhancement around Au NPs, which can increase light absorption of surrounding dye molecules in a dye-loaded film. Therefore, enhancement of light harvesting efficiency and hence photocurrent of a DSSC can be expected using such Au-TiO_2 photoanode.

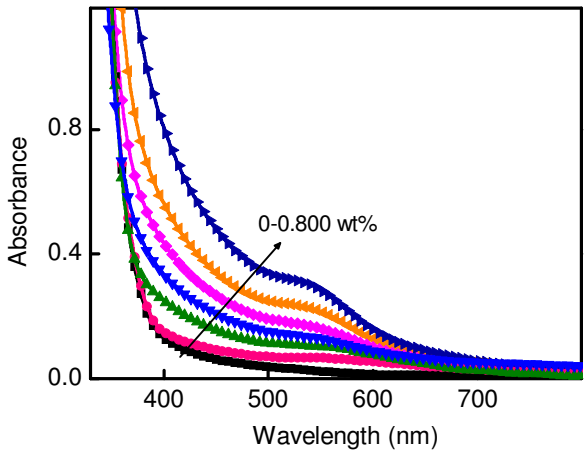

Figure 3. Spherically integrated UV-vis absorption spectra of Au-TiO_2 films (~1 μm) with different Au contents.

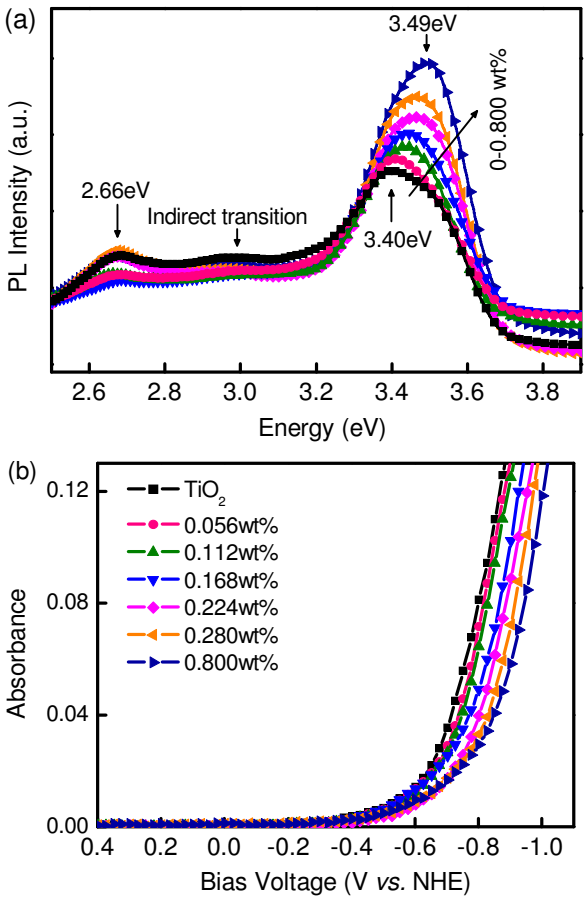

Figure 4. (a) Photoluminescence spectra of pure TiO_2 and Au-TiO_2 films with different Au contents and (b) optical absorbance at 780 nm of the TiO_2 films with different Au loadings measured as a function of the applied potential in acetonitrile containing 0.1 M $LiClO_4$. The scan rate is 12.5 mV/s.

Photoluminescence (PL) spectra of Au-TiO_2 films with different Au loadings under an excitation of the 280 nm line of a Xe lamp, Figure 4a, record the effect of Au-inlay on the energy-

band structure of Au-TiO_2 nanocomposites. The peaks at 2.66 eV originate from the radiative transitions from the localized excitons in oxygen-defect levels and the emissions located at about 2.98 eV are assigned to the indirect transitions, both of them have no substantial changes. However, the highest energy direct transition, namely the band edge luminescence,[55] moves toward higher energy with the increase of Au loading. The shifts of the peak position indicate that the band gap is enlarged by the Au-inlay and it gradually becomes wider as the Au content increases. The enlarged band gap is likely attributed to the negative shift of CB, which can be interpreted as a natural consequence of the related upward shift of the equivalent Fermi level of Au-TiO_2 nanocomposites. The CB edge is sensitive to the surface property of TiO_2, which can be affected by the interaction between Au and TiO_2 NPs.

The quasi-Fermi level (E_F) of TiO_2 is directly related to the CB edge and free electron density (n_c) in the CB as illustrated in the following expression,[56]

$$E_F = E_{CB} + k_B T \ln \frac{n_c}{N_c}$$

in which E_{CB} is the conduction band energy level, k_B is the Boltzmann constant, T is the absolute temperature, and N_c is the density of states in the conduction band of TiO_2. As more electrons are accumulated within the CB of TiO_2, the quasi-Fermi level becomes more negative and shifts closer to the conduction band edge of TiO_2. Under equilibrium conditions, the quasi-Fermi level (E_F) of semiconductor nanoparticles can be determined by the flat-band potential (V_{FB}) of the semiconductor nanoparticles.[57] Making use of this principle, it can be extended to probe the effect of Au-inlay on the quasi-Fermi level of the Au-TiO_2 nanocomposites and the extent to which it shifts to the more negative potentials. By using the spectroscopic technique developed by Fitzmaurice and Grätzel,[58] the flat-band potential of the TiO_2 and Au-TiO_2 nanocomposites were determined, as shown in Figure 4b. As the applied potential becomes more negative, electrons accumulate near the semiconductor/electrolyte interface and the absorbance increases. The onset potential of absorbance is regarded as the flat band potential. Clearly, in the absence of Au, the obtained V_{FB} is about -0.65 V versus normal hydrogen electrode (NHE), which is similar to the reported value.[59] While for Au-inlaid TiO_2 nanocomposites, a gradual negative shift of flat-band potential is observed, for example, by 30 mV for 0.056 wt% and by 170 mV for 0.800 wt% Au/TiO_2. The V_{FB} of the electrode material in DSSCs is important as the open-circuit photovoltage (V_{oc}) is determined by the difference between the redox potential of electrolyte and the quasi-Fermi level of the anode, which increases linearly with the V_{FB} for a given redox couple.[60,61] The negatively shifted V_{FB} means a shift away from the redox potential, thereby an increase in V_{oc}.

Owing to the above desirable physicochemical properties, TiO_2 and Au-TiO_2 as working electrodes are constructed in DSSCs and the photovoltaic performances under simulated AM1.5G illumination (100 mW cm^{-2}) are studied. As photocurrent generation depends on electron injection that is determined by the energy level difference (driving force for electron injection) between the excited energy level (approximately estimated by the lowest unoccupied molecular orbital, LUMO) of the dye molecule and the CB edge of TiO_2, it is wise to select a dye that have sufficiently high LUMO to guarantee efficient electron injection in DSSCs with Au-TiO_2 photoanode. Although the N719 dye is an outstanding dye in DSSCs, its LUMO (-0.65 V) is not high enough,[2] thereupon, a D-π-A structured metal-free organic dye sensitizer (**FNE29**, Figure S5), whose LUMO (-0.92 V) is 0.27 V more negative than that of N719, is designed and synthesized for this study.

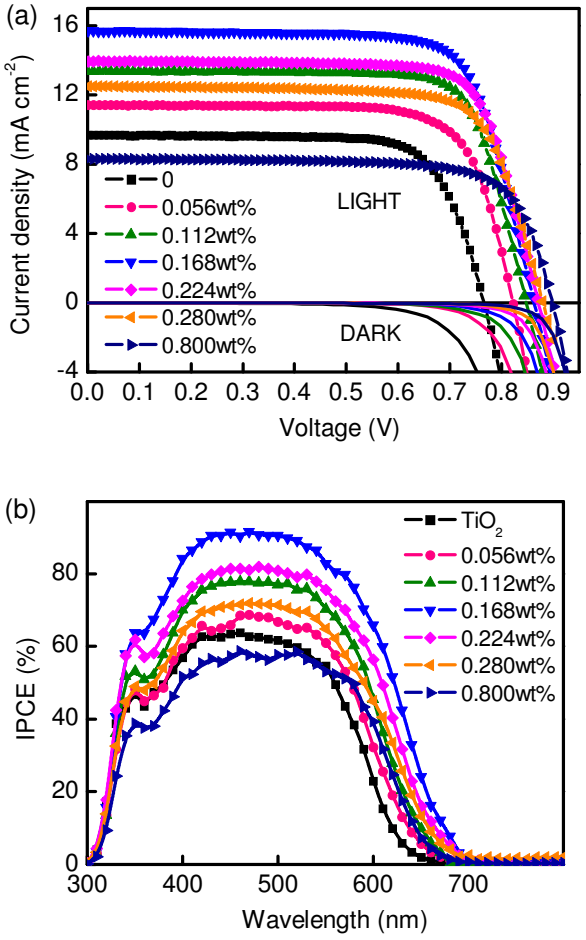

Figure 5. (a) *J-V* characteristics of the DSSCs based on **FNE29** sensitized pure TiO_2, or Au-TiO_2 (Au/TiO_2 = 0.056wt%, 0.112wt%, 0.168wt%, 0.224wt%, 0.280wt%, and 0.800wt%) films under 100 mW cm^{-2} AM1.5G illumination and (b) IPCE spectra of the above DSSCs.

Photocurrent density (J) – voltage (V) characteristics of DSSCs containing **FNE29** sensitized Au-TiO_2 photoanodes with different Au loadings were measured under AM1.5G illumination (100 mW cm^{-2}) and under dark. By repeating experiments, the optimal thickness of Au-TiO_2 anode for high efficiency DSSCs is ~4 μm. Based on 4-μm-thick Au-TiO_2 anodes, several parallel cells for each ratio of Au/TiO_2 are tested, and the relative deviation for each photovoltaic parameter is less than 5%. Figure 5a plots the *J-V* curves for each single best cell and the corresponding photovoltaic parameters are summarized in Table 1, showing that the presence of Au NPs and its loading amount largely affect the photovoltaic performances. With the weight ratio of Au/TiO_2 ranging from 0 to 0.800 wt%, short-circuit photocurrent density (J_{sc}) first increases from 9.66 mA/cm^2 (0

wt%), reaches a maximum value (15.7 mA/cm^2, a factor of 1.5 relative to the value for 0 wt% Au/TiO_2) at 0.168 wt%, and then decreases gradually with further increasing the Au content. By contrast, V_{oc} always keeps increasing and was measured to be 897 mV when the mass ratio reaches 0.800 wt%, which is very close to the theoretical maximum voltage (~950 mV)[62] and 131 mV greater than the value for the cell based on pure TiO_2 (766 mV). Fill factor (FF) changes slightly within the tested range. As a consequence, power conversion efficiency (η) rises, peaks and then falls with the increasing ratio of Au/TiO_2. As summarized in Table 1, compared with the efficiency of 5.5% (V_{oc} = 766 mV, J_{sc} = 9.66 mA cm^{-2}, FF = 0.744) for the cell based on pure TiO_2 anode, an unprecedented efficiency of 10.1% (V_{oc} = 863 mV, J_{sc} = 15.71 mA cm^{-2}, FF =0.742) has been achieved for Au-TiO_2 based cell at the Au/TiO_2 ratio of 0.168 wt%, in which J_{sc} is increased by 63% and V_{oc} is lifted by 97 mV, resulting in enhancement of power conversion efficiency by 84%. Deserved to be mentioned, the 10.1% efficiency obtained on 4-μm-thick 0.168 wt% Au-TiO_2 anode here is even much higher than the optimal efficiency of 6.8% (V_{oc} = 750 mV, J_{sc} = 12.36 mA cm^{-2}, FF = 0.734) achieved on 14-μm-thick pure TiO_2 anode with other conditions being the same. Evidently, the optimal thickness towards solar cell performance has been reduced significantly from 14 to 4 μm by taking advantage of the unique properties of Au-TiO_2 nanostructures. To the best of our knowledge, this is the thinnest photoanode so far that yields efficiency higher than 10%.

Figure S6 shows the efficiency evolution of the Au-TiO_2 based DSSC subjected to aging for 26 days. The efficiency increased gradually after aging for 6 days and then remained constant from 6 to 10 days followed by a gradual decrease up to 26 days due to the electrolyte leakage. This indicates that Au NPs in our system were not dissolved in the electrolyte for at least 10 days. Otherwise, the efficiency would decrease with time. So far, we do not know the reason why Au NPs in this system are stable when exposed to the iodide/triiodide electrolyte. This interesting issue will be the focus of our future investigation.

Table 1. Photovoltaic performance parameters for DSSCs and the adsorbed dye amount on TiO_2.

Au/TiO_2 ratio	V_{oc} (mV)	J_{sc} (mA cm^{-2})	FF	η (%)	Adsorbed dye amount (10^{-8} mol cm^{-2} μm-1)
0	766	9.66	0.744	5.5	4.26
0.056wt%	821	11.40	0.746	7.0	2.73
0.112 wt%	847	13.37	0.769	8.7	2.57
0.168 wt%	863	15.71	0.742	10.1	2.42
0.224 wt%	871	12.85	0.761	8.5	2.07
0.280 wt%	880	11.50	0.743	7.5	1.66
0.800 wt%	897	8.30	0.746	5.6	1.21

The corresponding incident monochromatic photon-to-electron conversion efficiency (IPCE) spectra are shown in Figure 5b. Clearly, the maximum IPCE increases, reaches the maximum at 0.168 wt% Au/TiO_2 and then decreases with the increase of Au content, having the same trend with the variation of J_{sc}. An obvious feature of IPCE is the spectrum broadening to longer wavelength upon Au-inlay on TiO_2, which is attributable to the plasma resonance effect.

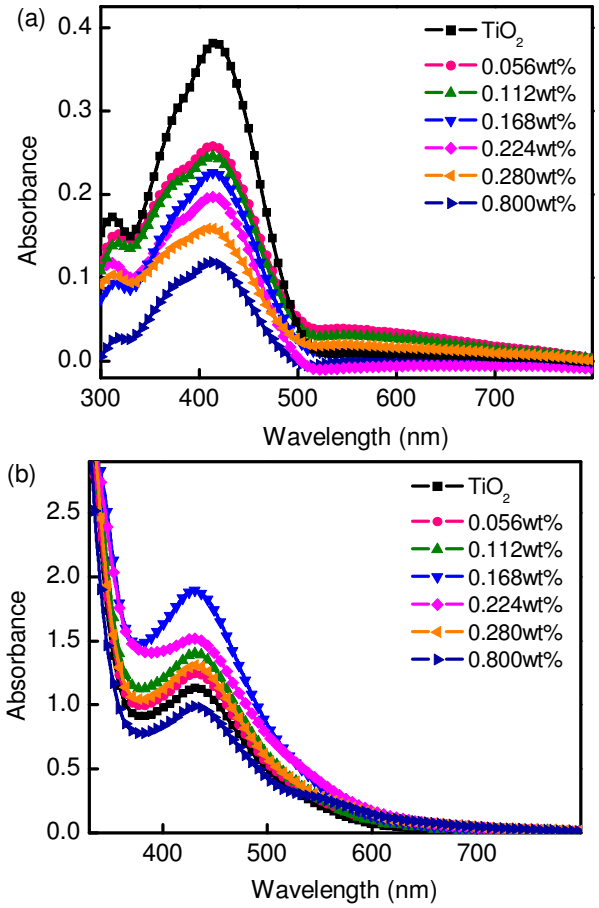

Figure 6. UV-vis absorption spectra of the desorbed FNE29 from dye-loaded TiO_2 films in THF/TBAOH solutions (a) and spherically integrated UV-vis absorption spectra of the FNE29-loaded TiO_2 films (b).

From the summarized photovoltaic parameters in Table 1, the enhancement of efficiency in the presence of Au arises from the increase in both V_{oc} and J_{sc}. Since Au NPs are directly inlaid in the surface of TiO_2, it is certain to decrease the active area of TiO_2 in contact with the dye molecules to some extent, which would decrease dye adsorption and hence IPCE. To elucidate the increase of J_{sc} and IPCE, dye adsorption was first measured by desorbing the dye into a tetrahydrofuran (THF)/tetrabutylammonium hydroxide (TBAOH) (v/v, 100:1) solution, whose UV-vis absorption spectra is shown in Figure 6a. The adsorbed dye amount is lowered by the presence of Au NPs and the decrease in dye adsorption becomes more pronounced with the increase of Au loadings (Table 1). Despite the decreased dye adsorption, the absorbance of the dye-loaded TiO_2 films increases with the Au amount up to 0.168 wt% Au/TiO_2 and then decreases with further increasing the Au amount (Figure 6b), being in good agreement with the changing tendency of the J_{sc} (Figure 5a) and the maximum IPCE (Figure 5b). The lower maximum IPCE for the cell with 0.800 wt% Au/TiO_2 anode than that for pure TiO_2 based cell should be attributed to its lower absorption owing to its lower dye adsorption. Comparison of Figure 6a with b reveals that the Au NPs plays a role of something like 'antenna' for the incident light that stores the incident solar energy in a localized surface plasmon mode. The resonant plasmon excitation of Au NPs can cause intense local

electromagnetic field enhancement around the Au NPs,[33] and thus enhance the absorption of the surrounding dye molecules remarkably (Scheme 1). As the Au NPs are inlaid on the TiO_2 surface and are thus very close to the dye molecules, the near field enhancement is very pronounced. By comparison of Figure 6a and b, the plasmon induced optical enhancement increases with the Au amount up to 0.168wt% Au/TiO_2 and then remains almost constant with further increasing the Au amount (Figure S7). Therefore, the decrease in absorbance with Au/TiO_2 above 0.168 wt% is ascribed to the much decreased dye adsorption. In consideration of both dye adsorption and local field enhancement, the highest light harvesting efficiency has been realized at 0.168 wt% Au/TiO_2, and the increase of J_{sc} together with the broadening of IPCE spectra would be attributed to the surface plasma effect of Au NPs.

The absorption onset of dye-loaded film (Figure 6b) located at 600-700 nm is basically consistent with the IPCE onset (Figure 5b). Compared to the weak absorption near the onset wavelength (Figure 6b), the corresponding IPCE values (Figure 5b) are larger than expected. This is likely attributed to the increased film thickness (from 1 μm for the UV-vis absorption measurement to 4 μm for the DSSC fabrication) and the significant surface plasma effect of Au NPs.

In Figure 5a, DSSCs with Au-TiO_2 photoanode all exhibit much higher V_{oc} and lower dark currents than that with pure TiO_2 anode. For DSSCs with a given redox electrolyte, the V_{oc} depends on the quasi-Fermi level of the anode. Undoubtedly, negatively shifted quasi-Fermi level of Au-TiO_2 nanocomposites which have been proved above can be the main factor in achieving higher V_{oc}. This can also be confirmed by the measured relative CB positions directly in DSSC devices using the method developed by Frank and coworkers.[63] Figure 7a shows V_{oc} as a function of charge density obtained by charge extraction[66] at open circuit under LED light (532 nm) with various intensities. Clearly, for all cases, the V_{oc} increases linearly with the logarithm of Q, and the slopes (m_c) are almost the same (176 mV). As compared to the DSSC with TiO_2 anode, V_{oc} increases gradually at a fixed Q with the increasing ratio of Au/TiO_2, indicating that the CB edge is shifted negatively and the shift becomes larger with the Au loading (listed in Table 2). The changing tendency of the measured CB edge in DSSCs is consistent with that of flat band potential for Au-TiO_2 nanocomposites in Figure 4b.

Furthermore, the lower dark currents and the gradually increased forward turn-on voltage of photoanode (see dark *J-V* curves in Figure 5a) confirms that the nanostructure of Au-inlaid TiO_2 NPs can effectively reduce the charge recombination at TiO_2/dye/electrolyte interfaces (shunt leak). To further demonstrate the effect on the increase in V_{oc} by incorporating Au-TiO_2 nanostructures in DSSCs, electron lifetime (τ) as a function of applied potential for the DSSCs are investigated, as shown in Figure 7b. It is seen that electron lifetime becomes longer with increasing the ratio of Au/TiO_2. τ for the cell with 0.168 wt% Au/TiO_2 is almost 60 times that for pure TiO_2. This indicates that the recombination rate of the conduction band electrons is retarded significantly by Au inlay.

Figure S8 shows the electron lifetime as a function of charge density at open circuit. For all cases, electron lifetime decreased with increasing Q following a power-law relation. At a given Q, electron lifetimes for the Au-TiO_2 based DSSCs were longer than that of pure TiO_2 based DSSC, indicating that charge recombination was suppressed by the Au-inlay on TiO_2 surface. At the same charge density, the electron lifetime increased gradually with Au/TiO_2 up to 0.224wt% and then remained hardly changed with further increasing the Au content. The electron lifetime for the best DSSC with 0.168wt% Au/TiO_2 was 29 times that for the DSSC based on pure TiO_2. The highest electron lifetime was observed in the range of 0.224-0.800wt% Au/TiO_2, which was ~78 times that for pure TiO_2 based DSSC at the same charge density.

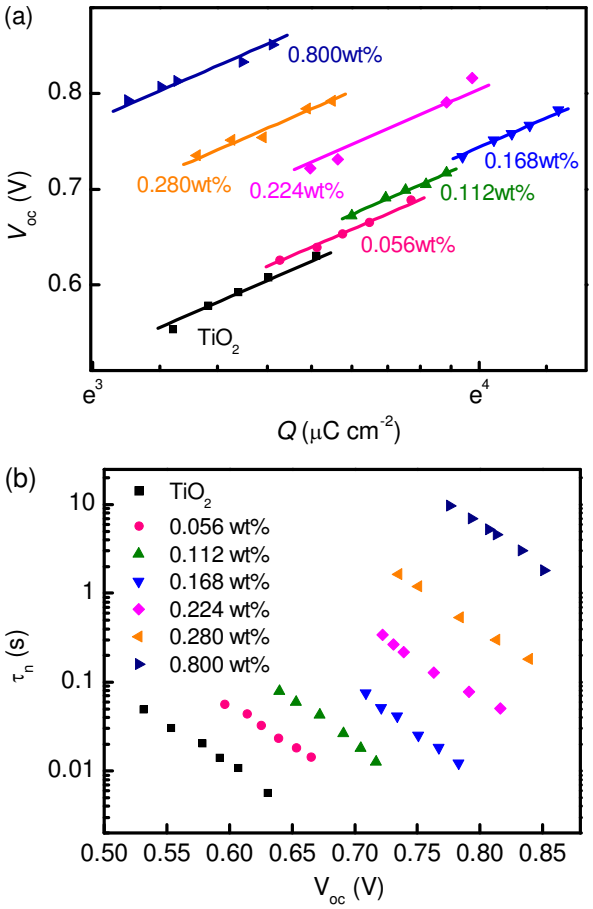

Figure 7. (a) V_{oc} as a function of charge density (Q) at open circuit for DSSCs based on **FNE29** sensitized pure TiO_2 or Au-TiO_2 (Au/TiO_2 = 0.056wt%, 0.112wt%, 0.168wt%, 0.224wt%, 0.280wt%, and 0.800wt%) films and (b) relationship of electron lifetime with charge density at open circuit for the DSSCs in (a).

The charge densities, which depend on the photo-injected electron density and electron lifetime at open circuit, are measured of 35.83 and 67.02 μC cm^{-2} for TiO_2 and Au-TiO_2 (0.168 wt%) based DSSCs, respectively, under 45 W m^{-2} LED light (532 nm). It is derived from Figure 7a that V_{oc} gain solely arising from the increased charge density by a factor of 1.87 is 110 mV. Therefore, the collective effects of the negatively shifted CB edge (43 mV) and increased charge density give enhancement of V_{oc} by 153 mV, which is in good agreement with the experimental V_{oc} enhancement (153 mV) under the same conditions. The contributions to V_{oc} enhancement arising from

CB edge shift and the change of charge density for all samples are summarized in Table 2.

Table 2. Contributions to V_{oc} gain *vs*. the experimental change of V_{oc}.

Au/TiO_2 ratio	ΔE_{CB} (mV)[a]	E_{FB} (V)	Q (μC cm^{-2})[b]	$m_c \ln[Q/Q(TiO_2)]$ (mV)[c]	$\Delta E_{CB} + m_c \ln[Q/Q(TiO_2)]$ (mV)	ΔV_{oc} (mV)[d]
0	0	0.65	35.83	0	0	0
0.056wt%	15	0.67	45.79	43	58	58
0.112wt%	31	0.70	50.18	59	90	87
0.168wt%	43	0.74	67.02	110	153	153
0.224wt%	104	0.77	53.65	71	175	186
0.280wt%	159	0.80	44.02	36	195	209
0.800wt%	248	0.84	32.00	-20	228	221

[a] $\Delta E_{CB} = E_{CB}$ (Au-TiO_2) - $E_{CB}(TiO_2)$ is obtained from Figure 7a. The positive value indicates a negative shift of CB and *vice versa*; [b] The charge density at open circuit was obtained at 45 W m^{-2} LED light (532 nm); [c] m_c is 176 mV obtained from Figure 7a; [d] $\Delta V_{oc} = V_{oc}$(Au-TiO_2) – $V_{oc}(TiO_2)$. The V_{oc} for the DSSCs is measured under illumination of LED light (532 nm, 45 W m^{-2}).

With the above data of CB edge negative shifts derived from the devices, it is necessary to analyze IPCE dependence on the Au loading. For the ratio of Au/$TiO_2 \leq 0.280$ wt%, although the CB edge is negatively shifted by 15-159 mV (Table 2), the maximum IPCE for Au-TiO_2 based DSSCs is larger than that for pure TiO_2 based DSSC, suggesting that electron injection is efficient. In this range of Au content, J_{sc} (Figure 5a) or maximum IPCE (Figure 5b) increases with light absorption (Figure 6b). However, for the 0.800 wt% Au-TiO_2 anode, the CB edge is negatively shifted by 248 mV, which may cause inefficient electron injection due to the much reduced driving force. This is likely another reason for its lower J_{sc} (Figure 5a) and maximum IPCE (Figure 5b) than those of pure TiO_2 based DSSC, respectively, besides the decreased dye adsorption.

For such Au-inlaid TiO_2 photoanodes, they are also appropriate for other dyes (Figure S9) with suitable LUMOs, and significant improvements of solar cell performances have been achieved in a similar way to **FNE29**, as shown in Table S1. Herein, **FNE29** dye is selected as a representative sensitizer for the above discussions.

Conclusions

In summary, Au-TiO_2 photoanodes with a mosaic structure of ~2 nm Au NPs directly inlaid in TiO_2 are designed and fabricated as the working electrode to construct DSSCs. In addition to the typical plasma-induced enhancement of the dye absorption for high photocurrent, it is demonstrated that the quasi-Fermi level of such Au-TiO_2 photoanodes can be modulated to more negative potentials by controlling the Au/TiO_2 weight ratio and the charge recombination rate can be reduced gradually with increasing the Au content to enlarge the photovoltage. As a consequence, an efficiency of 10.1% with the V_{oc} of 863 mV for the best DSSC in this study, which is very close to the theoretical maximum value (950 mV) for the I_3^-/I^- based DSSCs, has been achieved based on a 4-μm-thick Au-TiO_2 photoanode at 0.168 wt% ratio of Au/TiO_2. To the best of our knowledge, this is the first report that V_{oc} can be enhanced remarkably when Au NPs are incorporated in TiO_2 for construction of DSSCs.

Contrasting to the previous similar work reported in the literature,[36-45] we observed that the presence of Au NPs could induce a negative shift of CB edge and suppression of charge recombination besides the typical plasma effect. As a consequence, our Au-TiO_2 anode achieved a much higher V_{oc} than any other Au-TiO_2 anodes reported so far. This effect is likely caused by our preparation method, with which very small Au NPs are inlaid into TiO_2 and well dispersed on the surface of TiO_2 rather than in the pore channels. The intimate contact of Au NPs with TiO_2 may result in strong interaction between them and brings about such a novel effect.

These findings pave the way for optimizing solar cell performance and the efficiency greater than 10% obtained on such a thin film without a scattering layer is much desired for mass production of DSSCs.

Experimental Section

Synthesis of Cross-Linked Polymer. The cross-linked polymer (CLP) was prepared according to our previous report;[48] the synthetic route shown in Figure S1. Briefly, 4-vinyl benzyl chloride (8.40 g, 55 mmol), triphenylphosphorus (14.90 g, 57 mmol) and acetone (50 mL) were introduced into a dried flask and stirred at 45 °C under N_2 for 50 h. Being filtrated and washed with acetone, 4-vinylbenzyltriphenyl phosphorous chloride, a kind of phosphorous ionic liquid (PIL), was obtained as a white powder after drying overnight under vacuum at room temperature (yield: 85%). Then, the polymer (CLP) was prepared by conventional radical copolymerization of PIL and ethylene dimethacrylate (EDMA). After PIL (1.04 g, 2.5 mmol) together with EDMA (1.00 g, 5 mmol) and azobisisobutyronitrile (AIBN, 0.02 g, 0.12 mmol) were dissolved in 100mL methanol and stirred at 70 °C for 48 h, the mixture was poured into acetone and the precipitate was washed with THF and distilled water successively. By drying under vacuum at 70 °C for 12 h, the polymer (CLP) was obtained as a white powder (yield: 76%). The content of chlorine was determined by atomic absorption as 3.01%, the molar content of which was 8.7×10^{-4} mol g^{-1}.

Synthesis of Polymer Stabilized Au Colloid. After the CLP polymer (1.00 g) was dissolved in 30 mL methanol, 0.01 g $HAuCl_4$ was added to the solution under vigorous stirring. The

molar ratio of Au to chlorine was 1:5. Twenty minutes later, 4 mg of $NaBH_4$ in 10 mL methanol was added quickly to the above reaction system. The color changed immediately from yellow to red-brown, indicating the formation of Au NPs. The average diameter of the as-synthesized Au NPs was ~2 nm as revealed by TEM (Figure S2). The plasma absorption peak for the prepared gold colloid was located at 516 nm (Figure S3).

Fabrication of Nanocrystalline Au-TiO_2 Photoanodes. To incorporate the Au NPs into the TiO_2, the as-synthesized polymer stabilized Au NPs were first precipitated by centrifugation and then re-dispersed in methanol through ultrasonication. Afterwards, the mono-dispersed Au NPs colloid was directly blended into the titania paste[64] with different weight ratios (0–0.800 wt%) of Au/TiO_2, and various pastes containing TiO_2 and Au NPs were obtained after vigorous mixing. TiO_2 and Au-TiO_2 films were prepared on FTO with a doctor-blade method. The photoanodes were sintered at 500 ^oC for 2 h with a heating rate of 5 ^oC min^{-1}.

Synthesis of D-π-A structured Organic Dye. The organic dye **FNE29** (Figure S5a), 2-cyano-3-[5"-(4-(diphenylamino)phenyl)-3',3",4-tri-n-hexyl-[2,2',5',2"]terthiophene]acrylic acid **FNE29**, was prepared according to a previous method.[2] The UV-vis absorption spectrum of the dye in THF is shown in Figure S4b. ^1H NMR (400 MHz, CD_2Cl_2, δ): 8.32 (s, 1H), 7.29-7.31 (br, 2H), 7.17 (t, J = 7.2 Hz, 4H), 6.81-7.01 (m, 11H), 2.63-2.70 (m, 6H), 1.47-1.54 (m, 6H), 1.10-1.30 (m, 18H), 0.73-0.78 (m, 9H); ^{13}C NMR (100 MHz, CD_2Cl_2, δ): 153.68, 140.89, 122.79, 122.71, 122.34, 121.21, 119.61, 118.94, 118.08, 116.80, 116.70, 35.11, 33.57, 25.33, 25.31, 25.22, 25.20, 23.97, 23.77, 23.73, 23.69, 23.66, 23.64, 23.61, 23.59, 23.58, 23.29, 23.22, 22.86, 22.83, 22.77, 22.71, 22.62, 16.13, 14.69, 14.54, 14.47, 13.90, 13.86, 13.81, 11.30. ESI-Mass (m/z): $[M-H]^-$ calcd for $C_{96}H_{92}N_4O_8S_7$, 837.4; found, 837.4.

Solar Cell Fabrication. The dye **FNE29** sensitized TiO_2 and Au-TiO_2 films were used as the photoanodes of the cell. Counter electrodes were prepared by drop-casting a 5 mM solution of H_2PtCl_6 in ethanol on the FTO substrates followed by heat treatment at 380 ^oC for 30 min. The dye-sensitized TiO_2 photoanode and the counter electrode were separated by a hot-melt Surlyn film (30-μm-thick) and sealed through hot-pressing. The redox electrolyte (0.1 M LiI, 0.05 M I_2, 0.6 M 1,2-dimethyl-3-n-propylimidazolium iodide, and 0.5 M 4-tert-butylpyridine in anhydrous acetonitrile) was injected into the interspace between the photoanode and counter electrode. Finally, the holes on the back of counter electrode were sealed with a Surlyn film covered with a thin glass slide under heat.

Photovoltaic Measurements. The photocurrent density-voltage curves of DSSCs were recorded on a Keithley 2400 source meter under the illumination of AM1.5G simulated solar light coming from an AAA solar simulator (Newport-94043A) equipped with a Xe lamp (450 W) and an AM1.5G filter. The light intensity was calibrated using a reference Si solar cell (Newport-91150) equipped with a KG-5 filter (Schott) in order to reduce the mismatch between simulated light and standard AM1.5G solar light in the region of 350-700 nm to less than 2%. Anti-reflection film was not used to reduce the incident light losses. A black mask with an aperture area of 0.2304 cm^2 was applied on the surface of DSSCs to avoid stray light completely. Action spectra of IPCE for the solar cells were obtained with an Oriel-74125 system (Oriel Instruments). The intensity of monochromatic light was measured with a Si detector (Oriel-71640).

Characterizations. Zeta potentials (ζ) of the colloids were measured by Malvern Zetasizer Nano ZS90 (Malvern instruments Ltd., UK) according to the Smolochowski equation. Each sample was analyzed in triplicate with deviation less than 1 mV. X-ray diffraction (XRD) profiles were recorded on an X-ray powder diffractometer (D8 Advance, Bruker) with Cu Kα radiation (λ = 0.154 nm). The UV-vis absorption spectra were measured on a Shimadzu UV-2550 UV-Vis spectrometer with an integrating sphere detector. The morphology and microstructure of the composite films were examined by high resolution transmission electron microscopy (HRTEM, JEM-2100F, JEOL). The film thickness was measured using a step profiler (Veeco Dektak 150, USA). Raman spectra were recorded using a Dilor LabRam-1B spectrometer, operating at a resolution of 1 cm^{-1}. The Spectra Physics model 164 argon ion laser was operated at 632.8 nm with about 6 mW of power. Photoluminescence spectra were obtained on a Shimadzu spectrofluorophotometer RF-5301PC with a Xe lamp as the excitation light source. X-ray photoelectron spectroscopy (XPS) experiments were carried out on a RBD upgraded PHI-5000C ESCA system (Perkin Elmer) with Mg Kα radiation (hν = 1253.6 eV). The charge extraction analysis was carried out on an electrochemical workstation (Zahner XPOT, Germany), which includes a green light emitting diode (LED, 532 nm) and the corresponding control system. The intensity-modulated spectra were measured at room temperature with light intensity ranging from 0.5 to 45 W m^{-2}, in modulation frequency ranging from 0.1 Hz to 10 kHz, and with modulation amplitude less than 5% of the light intensity. Optical electrochemistry was carried out using a typical three-electrode cell made of quartz, in which the Au-TiO_2 film, a platinum wire, and a silver wire were employed as working, counter, and quasi-reference electrodes, respectively. The supporting electrolyte was 0.1 M $LiClO_4$ in dry acetonitrile, which was deaerated with ultra-pure nitrogen for 15 min before measurement. The potential of the silver wire was calibrated with ferrocene. The cell was incorporated into the sample compartment of a Shimadzu UV-2550 UV-Vis spectrometer. The potential scan was controlled with an electrochemical workstation (Zahner XPOT, Germany).

Acknowledgment

This work is funded by the National Basic Research Program (2011CB933302) of China, National Natural Science Foundation of China (20971025, 50903020, and 90922004), STCSM (12JC1401500), Jiangsu Major Program (BY2010147), Shanghai Leading Academic Discipline Project (B108).

Notes and references

† Department of Chemistry, Lab of Advanced Materials, Fudan University, 2205 Songhu Road, Shanghai 200438, P. R. China
‡ Present address: Key Laboratory of Atomic and Molecular Physics & Functional Materials of Gansu Province, College of Physics and Electronic Engineering, Northwest Normal University, 967 Anning East Road, Lanzhou 730070, P. R. China
□ These authors contributed equally to this work.

* Corresponding author. E-mail: zs.wang@fudan.edu.cn

§ Electronic Supplementary Information (ESI) available: See DOI: 10.1039/b000000x/

1. B. O'Regan, M. Grätzel, *Nature* 1991, **353**, 737-740.
2. M. K. Nazeeruddin, A. Kay, I. Rodicio, R. Humphry-Baker, E. Müller, P. Liska, N. Vlachopoulos, M. Grätzel, *J. Am. Chem. Soc.* 1993, **115**, 6382-6390.
3. N. Koumura, Z.-S. Wang, S. Mori, M. Miyashita, E. Suzuki, K. Hara, *J. Am. Chem. Soc.* 2006, **128**, 14256-14257.
4. S. Kim, J. K. Lee, S. O. Kang, J. Ko, J.-H. Yum, S. Fantacci, F. D. Angelis, D. D. Censo, Md. K. Nazeeruddin, M. Grätzel, *J. Am. Chem. Soc.* 2006, **128**, 16701-16707.
5. K.-L. Wu, C.-H. Li, Y. Chi, J. N. Clifford, L. Cabau, E. Palomares, Y.-M. Cheng, H.-A. Pan, P.-T. Chou, *J. Am. Chem. Soc.* 2012, **134**, 7488-7496.
6. F. Gao, Y. Wang, D. Shi, J. Zhang, M. Wang, X. Jing, R. Humphry-Baker, P. Wang, S. M. Zakeeruddin, M. Grätzel, *J. Am. Chem. Soc.* 2008, **130**, 10720-10728.
7. J.-H. Yum, D. P. Hagberg, S.-J. Moon, K. M. Karlsson, T. Marinado, L.-C. Sun, A. Hagfeldt, M. K. Nazeeruddin, M. Grätzel, *Angew. Chem. Int. Ed.* 2009, **48**, 1576-1580.
8. H.-N. Tian, Z. Yu, A. Hagfeldt, L. Kloo, L.-C. Sun, *J. Am. Chem. Soc.* 2011, **133**, 9413-9422.
9. J.-H. Yum, E. Baranoff, F. Kessler, T. Moehl, S. Ahmad, T. Bessho, A. Marchioro, E. Ghadiri, J.-E. Moser, C. Yi, M. K. Nazeeruddin, M. Grätzel, *Nat. Commun.* 2012, **3**, 631.
10. M.-K. Wang, N. Chamberland, L. Breau, J.-E. Moser, R. Humphry-Baker, B. Marsan, S. M. Zakeeruddin, M. Grätzel, *Nat. Chem.* 2010, **2**, 385-389.
11. T. Daeneke, T.-K. Kwon, A. B. Holmes, N. W. Duffy, U. Bach, L. Spiccia, *Nat. Chem.* 2011, **3**, 211-215.
12. P. Wang, S. M. Zakeeruddin, J. E. Moser, M. K. Nazeeruddin, T. Sekiguchi, M. Grätzel, *Nat. Mater.* 2003, **2**, 402-407.
13. H. Wang, X. Zhang, F. Gong, G. Zhou, Z.-S. Wang, *Adv. Mater.* 2012, **24**, 121-124.
14. M. Law, L. E. Greene, J. C. Johnson, R. Saykally, P.-D. Yang, *Nat. Mater.* 2005, **4**, 455-459.
15. D. Kim, A. Ghicov, S. P. Albu, P. Schmuki, *J. Am. Chem. Soc.* 2008, **130**, 16454-16455.
16. Y. H. Jang, X. Xin, M. Byun, Y. J. Jang, Z. Lin, D. H. Kim, *Nano Lett.* 2012, **12**, 479-485.
17. W. Guo, C. Xu, X. Wang, S. Wang, C. Pan, C. Lin, Z. L. Wang, *J. Am. Chem. Soc.* 2012, **134**, 4437-4441.
18. F. Huang, D. Chen, X. L. Zhang, R. A. Caruso, Y.-B. Cheng, *Adv. Funct. Mater.* 2010, **20**, 1301-1305.
19. B. Tan, E. Toman, Y. Li, Y. Wu, *J. Am. Chem. Soc.* 2007, **129**, 4162-4163.
20. P. J. Cameron, L. M. Peter, *J. Phys. Chem. B* 2005, **109**, 7392-7398.
21. S. Nakade, Y. Makimoto, W. Kubo, T. Kitamura, Y. Wada, S. Yanagida, *J. Phys. Chem. B* 2005, **109**, 3488-3493.
22. B. C. O'Regan, K. Walley, M. Juozapavicius, A. Anderson, F. Matar, T. Ghaddar, S. M. Zakeeruddin, C. Klein, J. R. Durrant, *J. Am. Chem. Soc.* 2009, **131**, 3541-3548.
23. S. A. Haque, E. Palomares, B. M. Cho, A. N. M. Green, N. Hirata, D. R. Klug, J. R. Durrant, *J. Am. Chem. Soc.* 2005, **127**, 3456-3462.
24. J. Bisquert, A. Zaban, M. Greenshtein, I. Mora-Seró, *J. Am. Chem. Soc.* 2004, **126**, 13550-13559.
25. G. Benkö, J. Kallioinen, J. E. I. Korppi-Tommola, A. P. Yartsev, V. Sundström, *J. Am. Chem. Soc.* 2002, **124**, 489-493.
26. A. Yella, H.-W. Lee, H. N. Tsao, C. Yi, A. K. Chandiran, M. Nazeeruddin, E. W.-G. Diau, C.-Y. Yeh, S. M. Zakeeruddin, M. Grätzel, *Science* 2012, **334**, 629-634.
27. H. J. Snaith, *Adv. Funct. Mater.* 2010, **20**, 13-19.
27. M. Danckwerts, L. Novotny, *Phys. Rev. Lett.* 2007, **98**, 026104.
28. K. Chen, C. Durak, J. R. Heflin, H. D. Robinson, *Nano Lett.* 2007, **7**, 254-258.
29. K. Kneipp, Y. Wang, H. Kneipp, L. T. Perelman, I. Itzkan, R. R. Dasari, M. S. Feld, *Phys. Rev. Lett.* 1997, **78**, 1667-1670.
30. R. Kumar, H. Zhou, S. B. Cronin, *Appl. Phys. Lett.* 2007, **91**, 223105.
31. P. K. Jain, X. Huang, I. H. El-Sayed, M. A. El-Sayed, *Acc. Chem. Res.* 2008, **41,** 1578–1586.
32. M. W. Knight, H. Sobhani, P. Nordlander, N. J. Halas, *Science*, 2011, **332**, 702-704.
33. Z. Liu, W. Hou, P. Pavaskar, M. Aykol, S. B. Cronin, *Nano Lett.* 2011, **11**, 1111-1116.
34. H. Li, Z. Bian, J. Zhu, Y. Huo, H. Li, Y. Lu, *J. Am. Chem. Soc.* 2007, **129**, 4538-4539.
35. A. P. Kuldarni, K. M. Noone, K. Munechika, S. R. Guyer, D. S. Ginger, *Nano Lett.* 2010, **10**, 1501-1505.
36. M. D. Brown, T. Suteewong, R. S. S. Kumar, V. D'Innocenzo, A. Petrozza, M. M. Lee, U. Wiesner, H. J. Snaith, *Nano Lett.* 2011, **11**, 438-445.
37. M. Li, S. K. Cushing, Q. Wang, X. Shi, L. A. Hornak, Z. Hong, N. Wu, *J. Phys. Chem. Lett.* 2011, **2**, 2125-2129.
38. J. Qi, X. Dang, *ACS Nano* 2011, **5**, 7108-7116.
39. I. Thomann, B. A. Pinaud, Z. Chen, B. M. Clemens, T. F. Jaramillo, M. L. Brongersma, *Nano Lett.* 2011, **11**, 3440-3446.
40. M. Ihara, K. Tanaka, K. Sakaki, I. Honma, K. Yamada, *J. Phys. Chem. B* 1997, **101**, 5153-5157.
41. C. Hägglund, M. Zäch, B. Kasemo, *Appl. Phys. Lett.* 2008, **92**, 013113.
42. K. Ishikawa, C. Wen, K. Yamada, T. Okubo, *J. Chem. Eng. Jpn.* 2004, **37**, 645-649.
43. S. D. Standridge, G. C. Schatz, J. T. Hupp, *Langmuir* 2009, **25**, 2596-2600.
44. J. F. Qi, X. N. Dang, P. T. Hammond, A. M. Belcher, *ACS Nano* 2011, **5**, 7108-7116.
45. H. Chio, W. T. Chen, P. V. Kamat, *ACS Nano* 2012, **6**, 4418-4427.
46. C. K. N. Peh, L. Ke, G. W. Ho, *Mater. Lett.* 2010, **64**, 1372-1375.
47. S. Standridge, G. Schatz, J. Hupp, *J. Am. Chem. Soc.* 2009, **131**, 8407-8409.
48. Y. Xiong, H. Wang, R. Wang, Y. Yan, B. Zheng, Y. Wang, *Chem. Commun.* 2010, **46**, 3399-3401.
49. N. Shibata, A. Goto, K. Matsunaga, T. Mizoguchi, S. D. Findlay, T. Yamamoto, Y. Ikuhara, *Phys. Rew. Lett.* 2009, **102**, 136105.
50. Y. L. Du, Y. Deng, M. S. Zhang, *J. Phys. Chem. Solids* 2006, **67**, 2405-2408.
51. J. C. Parker, R. W. Siegel, *Appl. Phys. Lett*. 1990, **57**, 943.
52. S. Cheng, Y. Wei, Q. W. Feng, J. B. Pang, S. A. Jansen, R. Yin, K. Ong, *Chem. Mater.* 2003, **15**, 1560-1566.
53. V. Idakiev, T. Idabakova, A. Naydenov, Z. Y. Yuan, B. L. Su, *Appl. Catal. B* 2006, **63**, 178-186.
54. A. Fujishima, K. Hashimoto, T. Watanabe, TiO_2 photocatalysis: fundamentals and applications, **1999**, *BKC: Tokyo*, P125.
55. N. Serpone, D. Lawless, R. Khairutdinov, *J. Phys. Chem.* 1995, **99**, 16646-16654.
56. M. Jakob, H. Levanon, P. V. Kamat, *Nano Lett.* 2003, **3**, 353-358.
57. M. T. Nenadović, T. Rajh, O. I. Mićić, *J. Phys. Chem.* 1984, **88**, 5827-5830.
58. G. Rothenberger, D. Fitzmaurice, M. Grätzel, *J. Phys. Chem.* 1992, **96**, 5983-5986.
59. G. Redmond, D. Fitzmaurice, *J. Phys. Chem.* 1993, **97**, 1426-1430.
60. J. Bandara, U. W. Pradeep, *Thin Solid Films* 2008, **517**, 952-956.
61. M. Kim, Y. Kwon, *J. Phys. Chem. C* 2009, **113**, 17176-17182.
62. Y. Ogomi, T. Kato, S. Hayase, *J. Photopolym. Sci. Technol.* 2006, **19**, 403-408.
63. G. Schlichthörl, S. Y. Huang, J. Sprague, A. J. Frank, *J. Phys. Chem. B* 1997, **101**, 8141-8155.
64. Z.-S. Wang, H. Kawauchi, T. Kashima, H. Arakawa, *Coord. Chem. Rev.* 2004, **248**, 1381-1389.